



# Numerical analyses of the sound absorption of three-dimensional MPP space sound absorbers

Toyoda, Masahiro  
Kobatake, Seiji  
Sakagami, Kimihiro

---

(Citation)

Applied Acoustics, 79:69-74

(Issue Date)

2014-05

(Resource Type)

journal article

(Version)

Accepted Manuscript

(URL)

<https://hdl.handle.net/20.500.14094/90001918>



# Numerical analyses of the sound absorption of three-dimensional MPP space sound absorbers

Masahiro Toyoda<sup>a</sup>, Seiji Kobatake<sup>b</sup>, Kimihiro Sakagami<sup>b</sup>

<sup>a</sup>*Department of Architecture, Faculty of Environmental and Urban Engineering, Kansai University,*

*3-3-35, Yamate-cho, Suita-shi, Osaka 564-8680, Japan*

<sup>b</sup>*Environmental Acoustics Laboratory, Graduate School of Engineering, Kobe University, Rokko, Nada, Kobe 657-8501 Japan*

---

## Abstract

Because microperforated panels (MPPs) can provide wide-band sound absorption without fibrous and porous materials, they are recognized as next-generation absorption materials. The fundamental absorbing mechanism is Helmholtz-resonance absorption due to the perforations and air-back cavity. Consequently, MPPs are usually placed in front of rigid-back walls. However, one of the authors has proposed MPP space sound absorbers without backing structures. Among these space absorbers, cylindrical MPP space absorbers and rectangular MPP space absorbers are advantageous due to their design flexibility and easy-to-use properties. Although their performances have been investigated experimentally, it is necessary to predict their absorption characteristics to develop improved shapes and efficient designs. Herein their absorption characteristics are numerically predicted using the two-dimensional boundary element method, and the applicability of a numerical method as a design tool to sufficiently predict the performance of MPP space absorbers

---

*Email address:* toyoda@kansai-u.ac.jp (Masahiro Toyoda)

is discussed.

*Keywords:* Sound absorption, MPP, Space sound absorber, BEM, Prediction

---

## 1. Introduction

A microperforated panel (MPP) is typically composed of a thin panel or film (less than 1-mm thick) with submillimeter holes and a perforation ratio of less than 1%. MPPs offer better sound absorption performance than ordinary perforated panels with larger perforations because the acoustic resistance and reactance of MPPs are suitable for sound absorption. The basic setup involves an MPP placed in front of a rigid-back wall with an air-back cavity in between, forming a Helmholtz resonator [1, 2, 3, 4].

One of the authors has proposed double-leaf MPP space sound absorbers (DLMPPs) [5, 6] and triple-leaf MPP space sound absorbers (TLMPPs) [7]. DLMPP has an air-cavity in between without a rigid-back wall, and TLMPP has a similar structure. A space sound absorber with an MPP and a permeable membrane without a backing structure has also been proposed [8]. The sound absorption characteristics and the effectiveness of these sound-absorbing structures have been examined theoretically and experimentally. DLMPP, TLMPP, and MPP-membrane space absorbers all have panel-like structures, which can be used as a sound absorbing panel or partition. However, the flat panel-like shape restricts their practical use in actual rooms or buildings.

To overcome these limitations, lightweight three-dimensional MPP space sound absorbers have been proposed [9, 10]. These space absorbers can be

easily hung from the ceiling or placed more freely on the floor. A cylindrical MPP space sound absorber (CMSA) and a rectangular MPP space sound absorber (RMSA), which are comprised of an MPP shaped in a cylindrical and rectangular shapes, respectively, have been proposed and investigated experimentally. CMSAs and RMSAs demonstrate moderate sound absorption performances similar to DLMPPs, and may be useful alternatives for sound absorbers in rooms and buildings.

Herein the absorption characteristics of CMSAs and RMSAs are numerically predicted using the two-dimensional boundary element method. The numerical results for the absorption coefficients are compared to those obtained by the reverberation chamber method [9, 10]. Based on the qualitative and quantitative comparisons, the accuracy of the prediction and the potential of the numerical method as a design tool for MPP space sound absorbers are discussed.

## 2. Formulation

### 2.1. Model

Two-dimensional calculation models are considered. Although three-dimensional models are better because CMSAs and RMSAs are three-dimensional space sound absorbers (Fig. 1, upper), a two-dimensional analysis may be sufficient because MPP structures generally have a higher absorption performance under plane waves with a normal incidence rather than other angles. Employing a two-dimensional model will dramatically reduce costs. Therefore, two-dimensional cylindrical and rectangular calculation models for CMSAs and RMSAs, respectively, are considered assuming an incident plane

wave with a unit amplitude and incident azimuth angle  $\theta$  (Fig. 1, lower).

## 2.2. Boundary integral equation

Region  $\Omega_1$  is considered to be bounded externally by  $\Sigma$  of center  $p$ , which is the sound receiver, and internally by  $\Gamma$  and small spheres  $\sigma_s$  and  $\sigma_p$ , which have respective centers  $s$  and  $p$  and small radii  $\epsilon$  (Fig. 2), where  $s$  is the sound source,  $q$  is a point on the boundary, and  $\mathbf{n}$  is the inward normal. Transmission admittance ratio  $A$  is assumed on  $\Gamma$ , and region  $\Omega_2$  is bounded externally by  $\Gamma$ . The time factor  $\exp(-i\omega t)$  is suppressed throughout, where  $i$  is an imaginary unit,  $\omega$  is the angular frequency, and  $t$  is time. Green's identity or integration by parts can be applied to region  $\Omega_1$  as,

$$\int_{\Omega_1} (f\nabla^2 g - g\nabla^2 f) dS = \int_{\Sigma+\sigma_s+\sigma_p+\Gamma} \left( f \frac{\partial g}{\partial \mathbf{n}} - \frac{\partial f}{\partial \mathbf{n}} g \right) dL, \quad (1)$$

where  $f$  and  $g$  are continuous and smooth functions, respectively. Substituting velocity potential  $\Phi$  and basic solution  $G$ , which satisfy the two-dimensional Helmholtz equation, for  $f$  and  $g$  respectively, yields the boundary integral equation for region  $\Omega_1$ . Basic solution  $G$  can be written as

$$G(\mathbf{r}_p, \mathbf{r}_q) = \frac{i}{4} \mathbf{H}_0^{(1)}(kr_{pq}) = \frac{i}{4} \{ \mathbf{J}_0(kr_{pq}) + i\mathbf{Y}_0(kr_{pq}) \}, \quad (2)$$

where  $\mathbf{r}$  is a position vector,  $k$  is the wavenumber, and  $r_{pq}$  is the distance between  $p$  and  $q$ .  $\mathbf{H}_0^{(1)}$ ,  $\mathbf{J}_0$ , and  $\mathbf{Y}_0$  are the Hankel function of the first kind of order zero, the Bessel function of order zero, and Neumann function of order zero, respectively. Taking the limit  $\epsilon \rightarrow 0$ , the integral over  $\sigma_s$  in Eq. (1) can be written as

$$\int_{\sigma_s} \left\{ \Phi(\mathbf{r}_q) \frac{\partial G(\mathbf{r}_p, \mathbf{r}_q)}{\partial \mathbf{n}_q} - \frac{\partial \Phi(\mathbf{r}_q)}{\partial \mathbf{n}_q} G(\mathbf{r}_p, \mathbf{r}_q) \right\} dL = \phi_d(\mathbf{r}_p), \quad (3)$$

where  $\phi_d$  is the velocity potential due to the direct wave from the sound source. Similarly, the integral over  $\sigma_p$  in Eq. (1) can be expressed as

$$\int_{\sigma_p} \left\{ \Phi(\mathbf{r}_q) \frac{\partial G(\mathbf{r}_p, \mathbf{r}_q)}{\partial \mathbf{n}_q} - \frac{\partial \Phi(\mathbf{r}_q)}{\partial \mathbf{n}_q} G(\mathbf{r}_p, \mathbf{r}_q) \right\} dL = -C(\mathbf{r}_p) \Phi(\mathbf{r}_p), \quad (4)$$

where  $C(\mathbf{r}_q)$  is the ratio of the included-part solid angle of  $\sigma_p$  in  $\Omega_1$  to  $4\pi$ ; if  $p$  is on a smooth boundary,  $C(\mathbf{r}_q) = 1/2$ . Assuming that  $\Sigma$  is a circle with an infinite radius and considering the Sommerfeld radiation condition [11], which can be expressed as

$$|r_{pq} \Phi(\mathbf{r}_q)| < K, \quad \sqrt{r_{pq}} \left\{ \frac{\partial \Phi(\mathbf{r}_q)}{\partial r_{pq}} - ik \Phi(\mathbf{r}_q) \right\} \rightarrow 0 \quad (r_{pq} \rightarrow \infty), \quad (5)$$

where  $K$  is a finite real number, the integral over  $\Sigma$  in Eq. (1) can be neglected. Consequently, substituting Eqs. (3) and (4) into Eq. (1) yields

$$\phi_d(\mathbf{r}_p) + \int_{\Gamma} \left\{ \phi_1(\mathbf{r}_q) \frac{\partial G(\mathbf{r}_p, \mathbf{r}_q)}{\partial \mathbf{n}_q} - \frac{\partial \phi_1(\mathbf{r}_q)}{\partial \mathbf{n}_q} G(\mathbf{r}_p, \mathbf{r}_q) \right\} dL = \frac{1}{2} \phi_1(\mathbf{r}_p) \quad (p \in \Gamma), \quad (6)$$

where  $\phi_1$  is the velocity potential on  $\Gamma$  of the  $\Omega_1$  side. Similarly, the boundary integral equation for region  $\Omega_2$  can be obtained as

$$- \int_{\Gamma} \left\{ \phi_2(\mathbf{r}_q) \frac{\partial G(\mathbf{r}_p, \mathbf{r}_q)}{\partial \mathbf{n}_q} - \frac{\partial \phi_2(\mathbf{r}_q)}{\partial \mathbf{n}_q} G(\mathbf{r}_p, \mathbf{r}_q) \right\} dL = \frac{1}{2} \phi_2(\mathbf{r}_p) \quad (p \in \Gamma), \quad (7)$$

where  $\phi_2$  is the velocity potential on  $\Gamma$  of the  $\Omega_2$  side. Letting  $v(\mathbf{r}_q)$  be the particle velocity at  $q$  leads

$$\frac{\partial \phi_1(\mathbf{r}_q)}{\partial \mathbf{n}_q} = \frac{\partial \phi_2(\mathbf{r}_q)}{\partial \mathbf{n}_q} = -v(\mathbf{r}_q) = -ikA(\mathbf{r}_q) \{ \phi_1(\mathbf{r}_q) - \phi_2(\mathbf{r}_q) \}. \quad (8)$$

Considering Eq. (8) and adding Eqs. (6) and (7), which are differentiated with regards to the normal on  $p$ , yields

$$\frac{\partial \phi_d(\mathbf{r}_p)}{\partial \mathbf{n}_p} + \int_{\Gamma} \left\{ \phi(\mathbf{r}_q) \frac{\partial^2 G(\mathbf{r}_p, \mathbf{r}_q)}{\partial \mathbf{n}_p \partial \mathbf{n}_q} \right\} dL = -ikA(\mathbf{r}_p) \phi(\mathbf{r}_p) \quad (p \in \Gamma), \quad (9)$$

where  $\phi = \phi_1 - \phi_2$ . Discretizing  $\Gamma$  with  $N$  constant elements, Eq. (9) can be approximately rewritten as

$$\frac{\partial \phi_{d,i}}{\partial \mathbf{n}_i} + \sum_{j=1}^N \phi_j \int_{\Gamma_j} \left\{ \frac{\partial^2 G(\mathbf{r}_i, \mathbf{r}_q)}{\partial \mathbf{n}_i \partial \mathbf{n}_q} \right\} dL = -ikA_i \phi_i \quad (i = 1, \dots, N), \quad (10)$$

where

$$\frac{\partial \phi_{d,i}}{\partial \mathbf{n}_i} = \frac{\partial e^{ik\{\mathbf{h}(\theta) \cdot \mathbf{r}_i\}}}{\partial \mathbf{n}_i} = ik\{\mathbf{h}(\theta) \cdot \mathbf{n}_i\} e^{ik\{\mathbf{h}(\theta) \cdot \mathbf{r}_i\}}, \quad (11)$$

$$\begin{aligned} \frac{\partial^2 G(\mathbf{r}_i, \mathbf{r}_q)}{\partial \mathbf{n}_i \partial \mathbf{n}_q} &= \frac{i}{4} \left[ k \frac{\mathbf{H}_1^{(1)}(kr_{\mathbf{p}_i \mathbf{q}})}{r_{\mathbf{p}_i \mathbf{q}}} \cos(\mathbf{n}_i, \mathbf{n}_q) \right. \\ &+ \left. \left\{ k^2 \mathbf{H}_0^{(1)}(kr_{\mathbf{p}_i \mathbf{q}}) - 2k \frac{\mathbf{H}_1^{(1)}(kr_{\mathbf{p}_i \mathbf{q}})}{r_{\mathbf{p}_i \mathbf{q}}} \right\} \cos(\mathbf{r}_{\mathbf{p}_i \mathbf{q}}, \mathbf{n}_i) \cos(\mathbf{r}_{\mathbf{p}_i \mathbf{q}}, \mathbf{n}_q) \right]. \quad (12) \end{aligned}$$

$\mathbf{h}(\theta) = (\sin \theta, -\cos \theta)$  in Eq. (11) is a unit vector that indicates the direction of the plane wave and  $\mathbf{p}_i$  in Eq. (12) is the center of  $i$ th element. In Eq. (10), the fourth-order Gauss-Legendre quadrature is employed to calculate the integral of Eq. (12) for  $i \neq j$ . For  $i = j$ , the integral, which has hyper singularity, is estimated with Terai's method [12] for a region of length  $\Delta L_j/3$  of center  $\mathbf{p}_i$  (Fig. 3) and the Gauss-Legendre quadrature for the other regions where  $\Delta L_j$  means the length of  $j$ th element. Potential differences  $\phi_i$  can be obtained by solving simultaneous equations of Eq. (10).

### 2.3. MPP admittance

Transmission admittance ratio  $A_i$  in Eq. (10) is given by Maa's theory [1] as

$$A_i = \rho_0 c_0 \left( \frac{1}{z_1} + \frac{1}{z_2} \right), \quad (13)$$

$$z_1 = \frac{1}{P} (z_{\text{resist}} + z_{\text{react}}), \quad (14)$$

$$z_{\text{resist}} = \frac{8\eta h}{(d/2)^2} \left( \sqrt{1 + \frac{X}{32}} + \frac{\sqrt{2}dX}{8h} \right), \quad (15)$$

$$z_{\text{react}} = -i\rho_0\omega h \left( 1 + \frac{1}{\sqrt{9 + (X^2/2)}} + \frac{0.85d}{h} \right), \quad (16)$$

$$X = \frac{d}{2} \sqrt{\frac{\rho_0\omega}{\eta}}, \quad (17)$$

$$z_2 = -i\omega\rho h, \quad (18)$$

where  $\rho_0$ ,  $c_0$ , and  $\eta$  are the density, sound speed, and viscosity coefficient of air, respectively.  $P$ ,  $h$ ,  $\rho h$ , and  $d$  are the perforation ratio, thickness, surface density, and hole diameter of an MPP, respectively.

#### 2.4. Dissipated energy ratio

Because sound can be transmitted through CMSAs and RMSAs, the sound absorption performance should be evaluated by the energy dissipated in the structures, which is expressed by the difference of the absorption and transmission coefficients,  $\alpha - \tau$ . Hereafter this difference in coefficients will be used to discuss the sound absorption performance. The average value of  $\alpha - \tau$  over all incident angles corresponds to the diffuse sound absorption coefficient measured in a reverberation chamber [13].  $\alpha - \tau$  is derived here using potential differences  $\phi_i$  obtained from Eq. (10). First, the dissipated acoustic energy in the  $j$ th element under a plane wave of incident angle  $\theta$  is expressed as

$$W_j(\theta) = \frac{1}{2} \text{Re} \{ p_j \cdot (-v_j)^* \} \Delta L_j, \quad (19)$$

where the asterisk denotes the complex conjugate.  $p_j$  is the sound pressure difference between the incident and transmitted sides of the MPP, which is



expressed as

$$p_j = \rho_0 \frac{\partial \phi_j}{\partial t} = -i \rho_0 \omega \phi_j. \quad (20)$$

$v_j$  is the particle velocity on the MPP surface, which is expressed as

$$v_j = i k A_j \phi_j. \quad (21)$$

Then the total dissipated energy can be rewritten as

$$W_a(\theta) = \sum_{j=1}^N W_j(\theta) = \frac{(\rho_0 \omega)^2}{2 \rho_0 c_0} \sum_{j=1}^N \text{Re} \{A_j\} |\phi_j|^2 \Delta L_j. \quad (22)$$

Next the incident energy into a CMSA can be given by

$$W_{\text{in}}(\theta) = \frac{(\rho_0 \omega)^2}{2 \rho_0 c_0} \frac{l_1}{\pi}, \quad (23)$$

where  $l_1$  is the perimeter of the circle. On the other hand, the incident energy into an RMSA can be written as

$$W_{\text{in}}(\theta) = \frac{(\rho_0 \omega)^2}{2 \rho_0 c_0} l_2 (\cos \theta + \sin \theta), \quad (24)$$

where  $l_2$  is the side length of the square. Consequently, considering the symmetric property of a CMSA, the dissipated energy ratio of a CMSA can be expressed as

$$\alpha - \tau = \frac{W_a(\theta)}{W_{\text{in}}(\theta)} = \frac{\pi}{l_1} \sum_{j=1}^N \text{Re} \{A_j\} |\phi_j|^2 \Delta L_j, \quad (25)$$

while that of the RMSA can be written as

$$\alpha - \tau = \frac{\int_0^{\pi/4} W_a(\theta) d\theta}{\int_0^{\pi/4} W_{\text{in}}(\theta) d\theta} = \frac{\int_0^{\pi/4} \sum_{j=1}^N \text{Re} \{A_j\} |\phi_j|^2 \Delta L_j d\theta}{l_2 \int_0^{\pi/4} (\cos \theta + \sin \theta) d\theta}. \quad (26)$$

### 3. Comparison and discussion on CMSAs

#### 3.1. CMSA with a 1-m perimeter placed on a floor

Figure 4 shows the numerical results of a CMSA with a 1-m perimeter ( $1/\pi$  m diameter) and the experimental results of a CMSA with a 1-m perimeter and 1-m height placed on a floor with and without a cover on the open end [9]. The MPP has a 0.5-mm hole diameter, 0.5-mm thickness, 0.785% perforation ratio, and 0.6-kg/m<sup>2</sup> surface density. The numerical results obtained by the two-dimensional boundary integral method and the experimental results agree well. The numerical results better correspond to the experimental results for a CMSA without a cover, suggesting that the two-dimensional numerical method can predict three-dimensional experiments due to the following:

- The energy dissipation of an MPP space absorber is mainly due to the inside resonance.
- Because the resonance can be considered as an infinite number of multiple reflections, many reflections yield a similar behavior to the resonance and a lot of energy dissipation. In contrast, few reflections yield less energy dissipation.
- For a three-dimensional case without a cover (Fig. 5), energy dissipation is smaller under the oblique incidence of elevation because many reflections are prevented.
- The impact of the results under the oblique incidence on the statistically averaged value becomes smaller because both the input and dissipated energy are smaller.

- Impact of the results under oblique incidence on the statistically averaged value becomes less because both input and dissipated energy are less.
- Consequently, the results under normal incidence are predominant.

The two-dimensional analysis can provide both qualitatively and quantitatively good predictions for CMSAs.

However, some discrepancies are observed below 500 Hz when there is a cover and at the dip around 630 Hz. For the case with a cover, the dissipated energy becomes larger than the prediction because the cover allows multiple reflections to occur more easily. In contrast, the discrepancy at the dip is attributed to the difference in the modal behavior; modal resonances occur only at discrete frequencies in the two-dimensional analysis, but, the resonances in the three-dimensional case occur under a normal incidence as well as an oblique incidence of elevation. For example, a wavelength projected on the horizontal plane under the  $38^\circ$  incidence of elevation at 630 Hz is very close to that under a normal incidence at 800 Hz, where the resonance occurs in the two-dimensional analysis. Thus, the resonance peaks become broad and the dip is compensated for in the experimental results. To overcome these discrepancies, three-dimensional analysis is necessary.

### *3.2. CMSA with a 1-m perimeter suspended off the floor*

Figure 6 shows the numerical results and the experimental results of a CMSA that is not directly placed on the floor (i.e., suspended from the ceiling) [9]. The parameters of the CMSA are the same as above. Although the prediction corresponds well to the measured data, the prediction accuracy

seems to be lower, especially below 500 Hz. This is because a CMSA placed on the floor can be considered as a double-height CMSA suspended from the ceiling, (i.e., a CMSA not directly set on the floor can be considered to have half of the height-perimeter ratio compared with that placed on the floor). Thus, the difference from the two-dimensional analysis where the height-perimeter ratio is infinite becomes larger, and consequently, the prediction accuracy is lower for a suspended CMSA.

As shown here, the shape difference between two- and three-dimensional cases can affect the prediction accuracy. Thus, the applicability of the prediction method proposed here can be determined by the height-perimeter ratio; for example, the height must be at least twice that of the perimeter for a sufficient prediction accuracy in the case where the CMSA is placed on the floor without a cover or must be larger than the perimeter for the case where the CMSA is not in direct contact with the floor. Consequently, the proposed method can be an effective prediction method for CMSAs regardless of the installation conditions as long as the height-perimeter ratio is considered.

### *3.3. CMSA with a 2-m perimeter placed on a floor*

Figure 7 shows the numerical results of a CMSA with a 2-m perimeter ( $2/\pi$  m diameter) and the experimental results of a CMSA with a 2-m perimeter and 1-m height placed on the floor with and without a cover on the open end [9]. The parameters of the MPP are the same as above. Although the prediction accuracy is not as good as that for the case of the 1-m perimeter, the accuracy is sufficient for practical designs. Obvious peaks are not observed in the experimental results, and the numerical results have two peaks due to inside resonances similar to the 1-m perimeter case, indicating

that the perimeter does not affect the absorption mechanism of a CMSA.

For a larger perimeter, multiple reflections are more difficult under an oblique incidence of elevation. Thus, the effect of the normal incidence becomes relatively strong (i.e., the numerical results obtained by the two-dimensional analysis can be close the experimental data). On the other hand, as discussed above, the prediction accuracy decreases because the height-perimeter ratio is smaller than the case with a 1-m perimeter and 1-m height. Consequently, the height-perimeter ratio dominates the absorption characteristics in this case.

#### 4. Comparison and discussion on RMSAs

##### *4.1. RMSA with a 1-m perimeter placed on the floor*

Figure 8 shows the numerical results of an RMSA with a 1-m perimeter (square with four 0.25-m sides) and the experimental results of an RMSA with a 1-m perimeter and 1-m height placed on the floor with and without a cover on the open end [10]. The parameters of the MPP are the same as those above. The fundamental trend is the same as that of a CMSA, and the numerical results agree well with the experimental ones. Therefore, the proposed prediction method can be effective regardless of the cross-sectional shape.

Although a dip between two resonance peaks is observed for CMSAs, an obvious dip is not seen in either the numerical or experimental results for the RMSA. Figure 9 directly compares a CMSA and an RMSA with 1-m perimeters. Although both MPPs have the same total length, the absorption performance of the RMSA is lower than that of the CMSA below 500 Hz

because the RMSA depends on the incident azimuth angle of the plane wave, while CMSA does not. Figure 10 shows the numerical results of the CMSA and the RMSA under normal and oblique incidences of  $22^\circ$  and  $45^\circ$ . Below a frequency of 500 Hz, the results of the RMSA under normal incidence are higher than those of the CMSA, while the results of the RMSA under oblique incidences are lower than those of the CMSA. Therefore, the RMSA has a lower total absorption performance than CMSA due to the following reasons:

- Generally an MPP shows the best absorption performance under a normal incidence because the energy dissipation decreases under an oblique incidence.
- As for an RMSA, the input energy is smallest under a normal incidence and largest under a  $45^\circ$  incidence.
- Thus, the absorption performance of an RMSA under a  $45^\circ$  incidence is poorer (Fig. 10).
- The impact of the  $45^\circ$  incidence on the dissipated energy under a random incidence is significant due to the largest input energy.

Consequently, the CMSA is stable under all incident angles and has an overall better performance than the RMSA. Additionally, the steepness of the dip between two resonance peaks for the RMSA changes according to the incident angle (Fig. 10). Therefore, random incidences compensate for the dip, and the discrepancy between the numerical and experimental results becomes relatively small at the dip unlike the CMSA case.

#### *4.2. RMSA with a 2-m perimeter placed on the floor*

Figure 11 shows the numerical results of an RMSA with a 2-m perimeter (square with four 0.5-m sides) and the experimental results of an RMSA with a 2-m perimeter and 1-m height placed on the floor with and without a cover on the open end [10]. The parameters of the MPP are the same as above. The numerical results do not correspond to the experimental ones as well as the 1-m case, but the accuracy is sufficient for a practical prediction. The tendency seems to be the same as the CMSA cases.

### **5. Conclusion**

Herein the efficiency of the prediction method by the two-dimensional boundary integral equation is investigated by comparing the numerical and experimental results of the dissipated energy ratio of CMSAs and RMSAs. Because the inner multiple reflections dominantly affect the energy dissipation, the dissipated energy is relatively small under the oblique incidence of elevation. Consequently, the total dissipated energy under a random incidence is determined due mostly to the normal incidence. Therefore, the absorption performance of three-dimensional space sound absorbers can be predicted sufficiently by a two-dimensional analysis, regardless of the installation conditions and cross-sectional shape. However, the height-perimeter ratio must be considered to realize a practical prediction accuracy.

Regardless of the height-perimeter ratio, the effects of a cover on the open end and a dip between the resonance peaks are not well predicted when the oblique incidence of elevation has a significant effect. To estimate the absorption characteristics of three-dimensional MPP space sound absorbers

in detail, a three-dimensional numerical analysis may be necessary.

## References

- [1] Maa DY. Theory and design of microperforated panel sound-absorbing constructions. *Scientia Sinica* 1975; 17: 55–71.
- [2] Maa DY. Microperforated-panel wideband absorber. *Noise Control Eng J* 1987; 29: 77–84.
- [3] Maa DY. Potential of microperforated panel absorber. *J Acoust Soc Am* 1998; 104: 2861–2866.
- [4] Maa DY. Practical single MPP absorber. *Int J Acoust Vib* 2007; 12: 3–6.
- [5] Sakagami K, Morimoto M, Koike W. A numerical study of double-leaf microperforated panel absorbers. *Appl Acoust* 2006; 67: 609–619.
- [6] K, Nakamori T, Morimoto M, Yairi M. Double-leaf microperforated panel space absorbers: A revised theory and analysis. *Appl Acoust* 2009; 70: 703–709.
- [7] Sakagami K, Yairi M, Morimoto M. Multiple-leaf sound absorbers with microperforated panels: an overview. *Acoust Australia* 2010; 38: 64–69.
- [8] Sakagami K, Nakamori T, Morimoto M, Yairi M. Absorption characteristics of a space absorber using a microperforated panel and a permeable membrane. *Acoust Sci Tech* 2011; 32: 47–49.

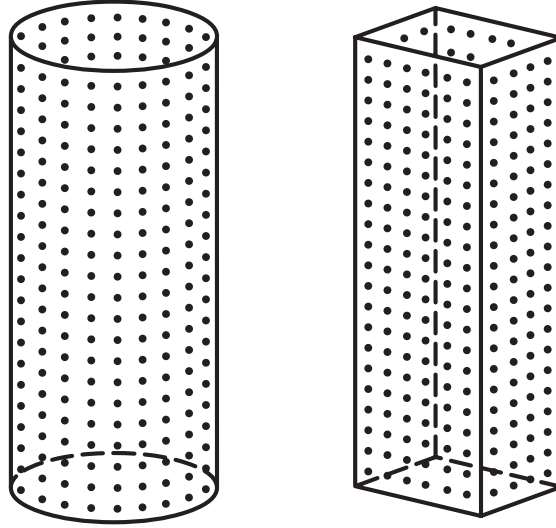


- [9] Sakagami K, Oshitani T, Yairi M, Toyoda E, Morimoto M. An experimental study on a cylindrical microperforated panel space sound absorber. *Noise Control Eng J* 2012; 60: 22–28.
- [10] Sakagami K, Yairi M, Toyoda E, Toyoda M. An experimental study on the sound absorption of three-dimensional MPP space sound absorbers: Rectangular MPP space sound absorbers (RMSA). *Acoust Australia* 2013; 41: 156–159.
- [11] Baker BB, Copson ET. The mathematical theory of Huygens principle 3rd edition. New York: Chelsea; 1987.
- [12] Terai T. On calculation of sound fields around three dimensional objects by integral equation methods. *J Sound Vib* 1980; 69: 71–100.
- [13] Sakagami K, Uyama T, Morimoto M, Kiyama M. Prediction of the reverberation absorption coefficient of finite-size membrane absorbers. *Appl Acoust* 2005; 66: 653–668.

## Figure captions

- Fig. 1.** Three- and two-dimensional models for a CMSA and an RMSA.
- Fig. 2.** Two-dimensional model to derive the boundary integral equation.
- Fig. 3.** Region where the hyper-singular kernel is estimated by Terai's method.
- Fig. 4.** Comparison between the numerical and experimental results for a CMSA with a 1-m perimeter placed on the floor.
- Fig. 5.** Cross-sectional schematic of the inner reflections for two-dimensional and three-dimensional CMSAs.
- Fig. 6.** Comparison between the numerical and experimental results for a CMSA with a 1-m perimeter suspended from a ceiling.
- Fig. 7.** Comparison between the numerical and experimental results for a CMSA with a 2-m perimeter placed on the floor.
- Fig. 8.** Comparison between the numerical and experimental results for an RMSA of 1-m perimeter placed on the floor.
- Fig. 9.** Comparison between the predicted results for a CMSA and an RMSA both with 1-m perimeters.
- Fig. 10.** Variation in the predicted results for a CMSA and an RMSA both with 1-m perimeters due to the incident angle.
- Fig. 11.** Comparison between the numerical and experimental results for an RMSA with a 2-m perimeter placed on the floor.

### Three-dimensional CMSA and RMSA



### Two-dimensional CMSA and RMSA

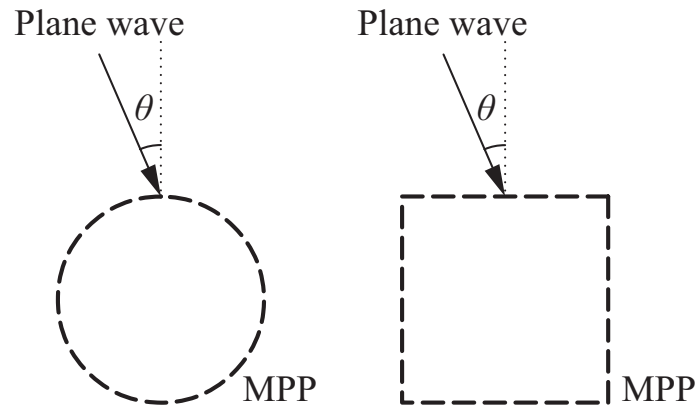


Figure 1: Three- and two-dimensional models for a CMSA and an RMSA.

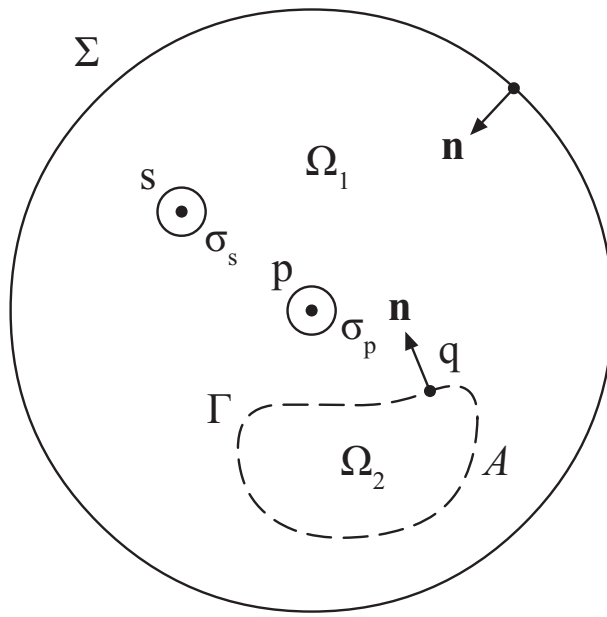


Figure 2: Two-dimensional model to derive the boundary integral equation.

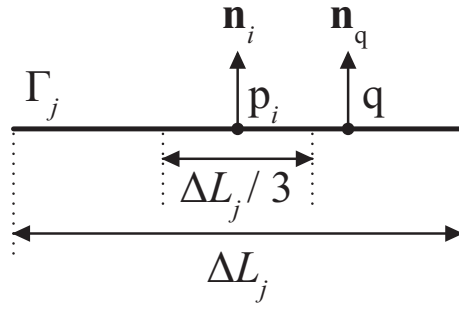


Figure 3: Region where the hyper-singular kernel is estimated by Terai's method.

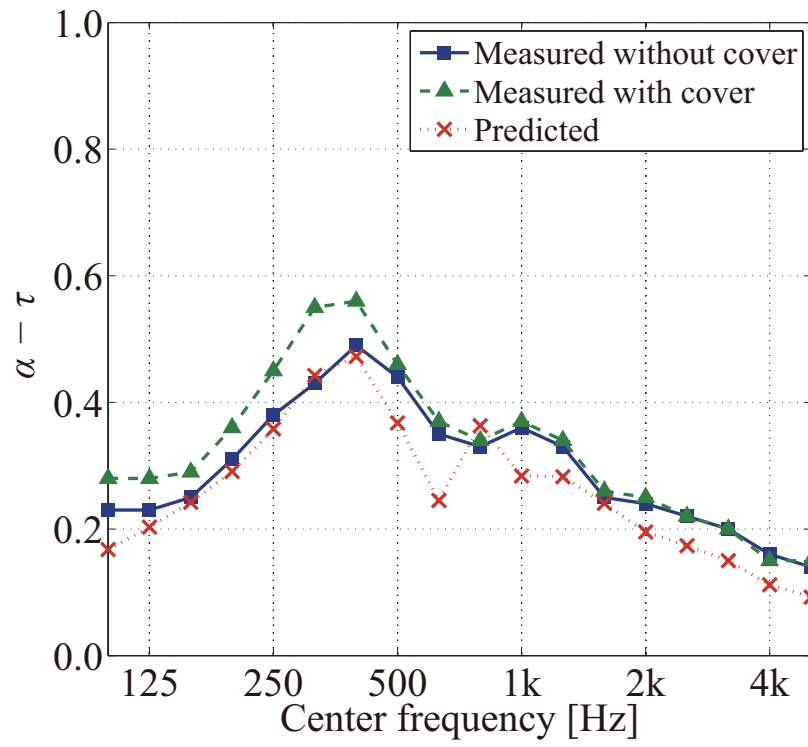


Figure 4: Comparison between the numerical and experimental results for a CMSA with a 1-m perimeter placed on the floor.

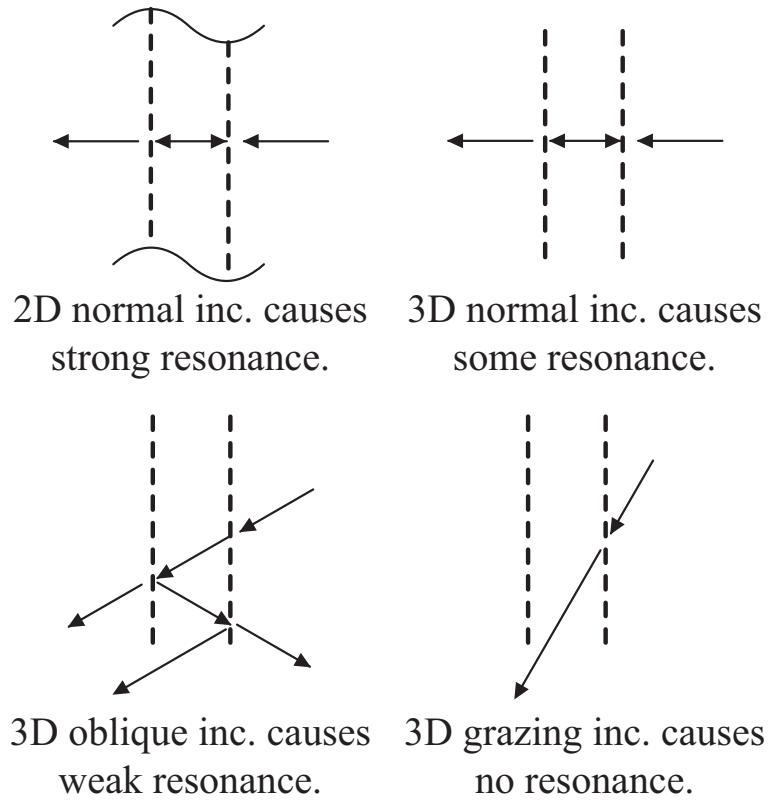


Figure 5: Cross-sectional schematic of the inner reflections for two-dimensional and three-dimensional CMSAs.

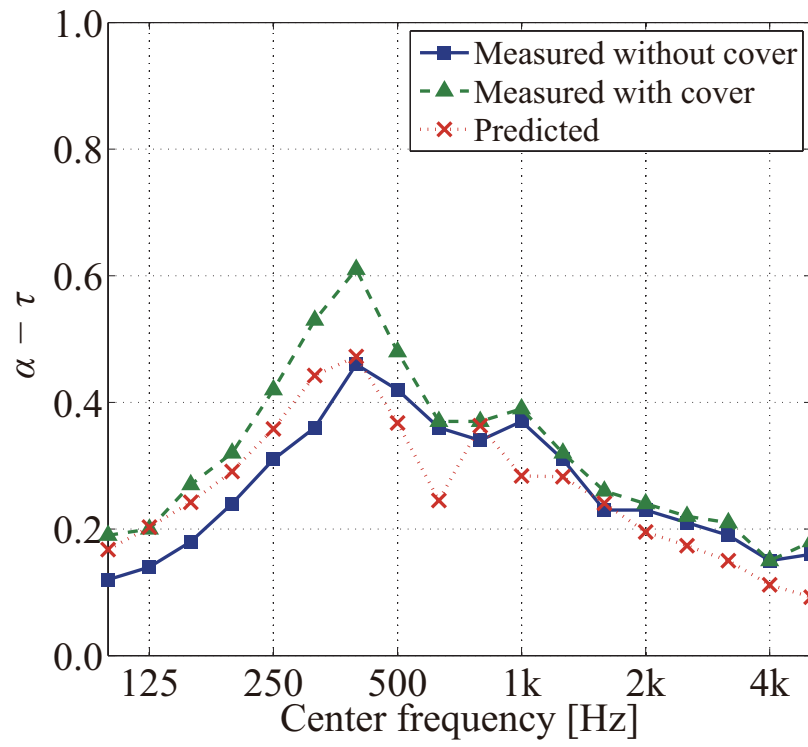


Figure 6: Comparison between the numerical and experimental results for a CMSA with a 1-m perimeter suspended from a ceiling.



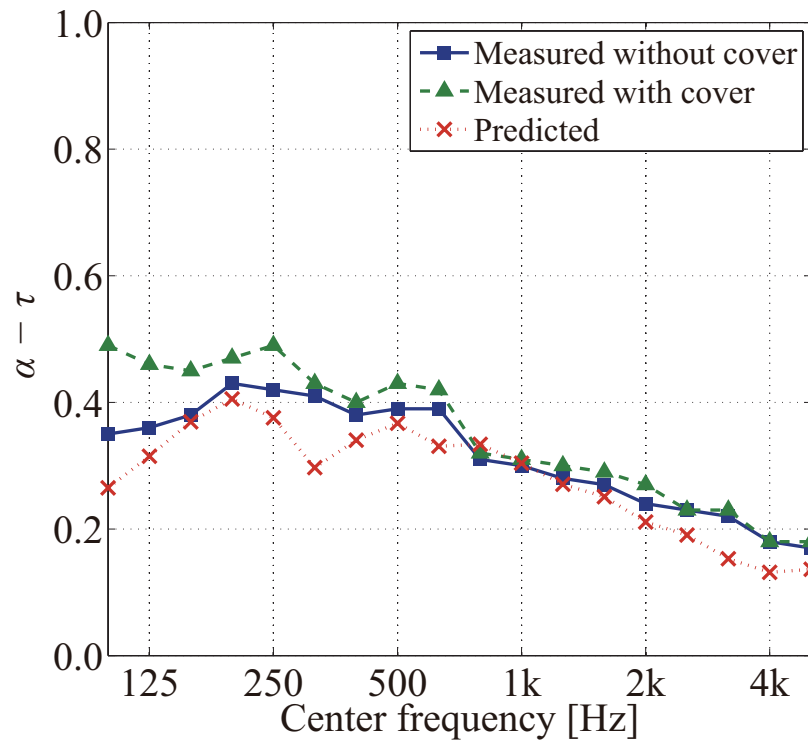


Figure 7: Comparison between the numerical and experimental results for a CMSA with a 2-m perimeter placed on the floor.

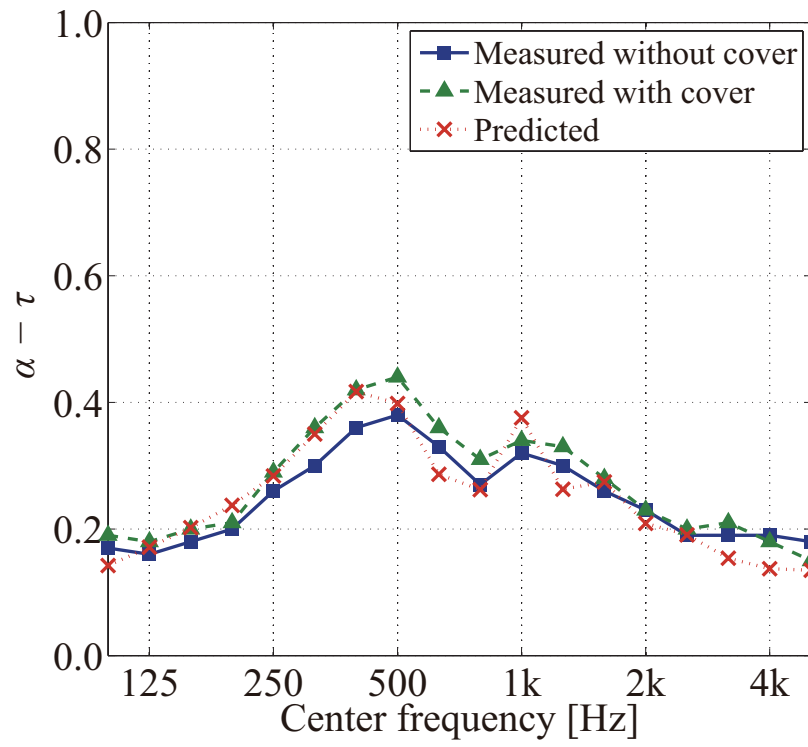


Figure 8: Comparison between the numerical and experimental results for an RMSA of 1-m perimeter placed on the floor.

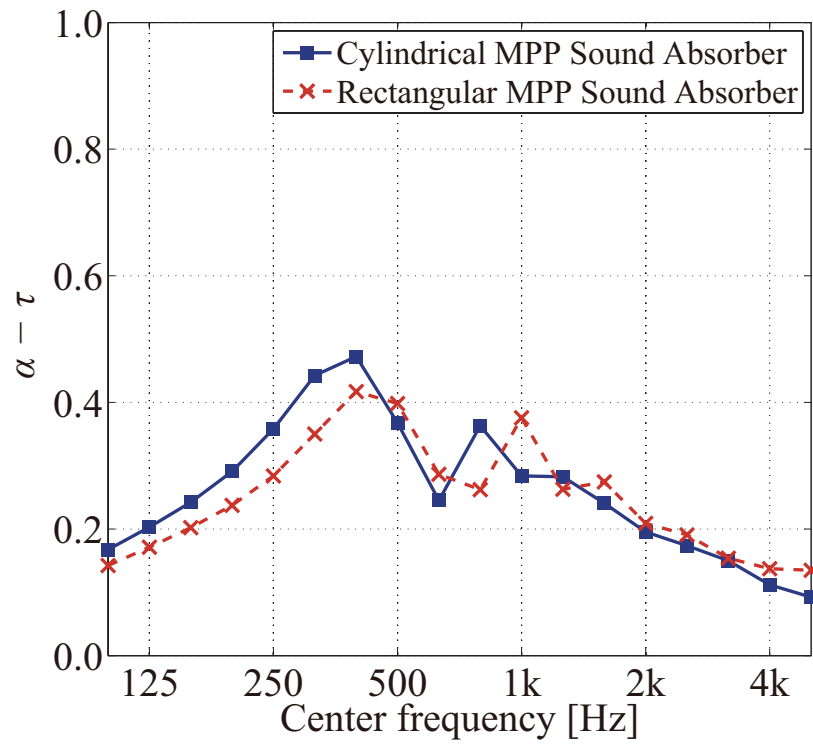


Figure 9: Comparison between the predicted results for a CMSA and an RMSA both with 1-m perimeters.

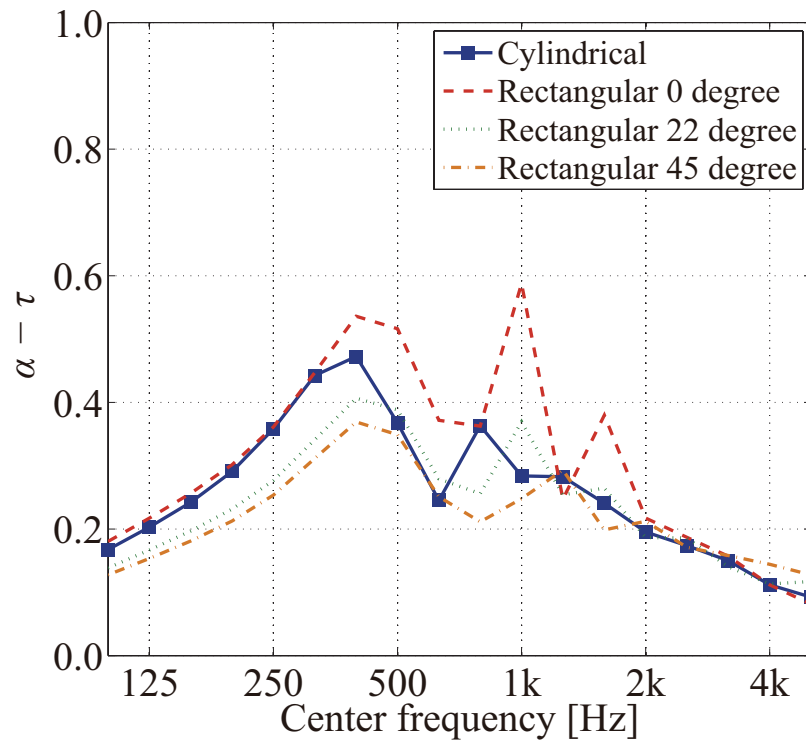


Figure 10: Variation in the predicted results for a CMSA and an RMSA both with 1-m perimeters due to the incident angle.

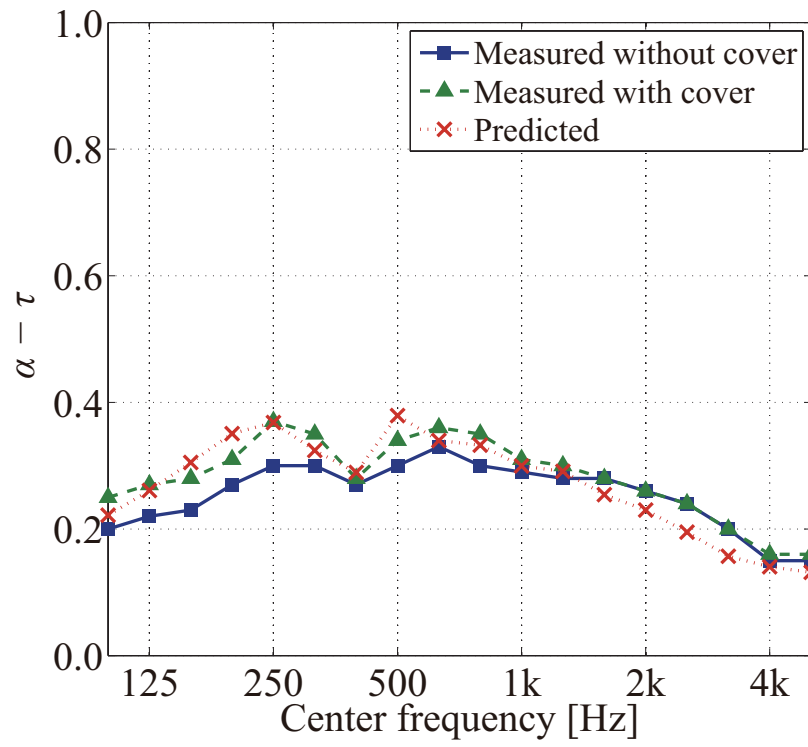


Figure 11: Comparison between the numerical and experimental results for an RMSA with a 2-m perimeter placed on the floor.